BONDI ACCRETION IN THE PRESENCE OF VORTICITY

Mark R. Krumholz

Physics Department, University of California, Berkeley, CA 94720; krumholz@astron.berkeley.edu

Christopher F. McKee

Departments of Physics and Astronomy, University of California, Berkeley, CA 94720; cmckee@astron.berkeley.edu

and

Richard I. Klein

Astronomy Department, University of California, Berkeley, CA 94720; and Lawrence Livermore
National Laboratory, P.O. Box 808, L-23, Livermore, CA 94550; klein@astron.berkeley.edu

ABSTRACT

The classical Bondi-Hoyle formula gives the accretion rate onto a point particle of a gas with a uniform density and velocity. However, the Bondi-Hoyle problem considers only gas with no net vorticity, while in a real astrophysical situation accreting gas invariably has at least a small amount of vorticity. We therefore consider the related case of accretion of gas with constant vorticity, for the cases of both small and large vorticity. We confirm the findings of earlier two-dimensional simulations that even a small amount of vorticity can substantially change both the accretion rate and the morphology of the gas flow lines. We show that in three dimensions the resulting flow field is nonaxisymmetric and time-dependent. The reduction in accretion rate is due to an accumulation of circulation near the accreting particle. Using a combination of simulations and analytic treatment, we provide an approximate formula for the accretion rate of gas onto a point particle as a function of the vorticity of the surrounding gas.

Subject headings: accretion, accretion disks — black hole physics — hydrodynamics — stars: formation —
stars: neutron

Online material: color figures

1. INTRODUCTION

Accretion of a background gas by a pointlike particle is a ubiquitous phenomenon in astrophysics, occurring on size scales ranging from black holes in galactic nuclei to individual stars or compact objects accreting the winds of their companions. Bondi, Hoyle, and Lyttleton (Hoyle & Lyttleton 1939, 1940a, 1940b, 1940c; Bondi 1952) treated this situation by considering the ideal problem of a massive point particle within a uniform gas moving at a constant speed with respect to the particle. For a polytropic gas, the problem is largely characterized by a single dimensionless parameter, the Mach number $\mathcal{M}$, which is defined as the ratio of the gas particle velocity to the sound speed of the uniform gas. (The ratio of specific heats, γ, also affects the accretion, but its effects are only of order unity.) The Bondi-Hoyle formula gives the approximate accretion rate as a function of $\mathcal{M}$, which, in a version updated by Ruffert (1994) and Ruffert & Arnett (1994), is

$$\dot{M}_{\mathrm{BH}} = 4\pi\rho_\infty G^2 M^2 c_\infty^{-3} \left[\frac{\lambda^2 + \mathcal{M}^2}{(1 + \mathcal{M}^2)^4} \right]^{1/2}. \quad (1)$$

Here, λ is a number of order unity that depends on $\mathcal{M}$ and on the equation of state. For $\mathcal{M} = 0$ (Bondi accretion) in an isothermal medium, $\lambda = \exp(1.5)/4 \approx 1.1$.

The Bondi-Hoyle formula finds wide application in astrophysics. Our first motivation for exploring this topic is star formation. The competitive accretion picture of star formation posits that protostars form with initially low masses, typically $\lesssim 0.1\,M_\odot$, and grow in mass by accreting unbound gas from the molecular clump in which they form (Bonnell et al. 1997, 1998,

2001a, 2001b; Klessen & Burkert 2000, 2001). The competition for gas is invoked to explain the initial mass function (IMF). This is a process of Bondi-Hoyle accretion, albeit in a turbulent medium, and one ought to be able to use a Bondi-Hoyle–like formula to estimate the rate at which the proposed "seed" protostars would accrete. A second significant area of application is in black holes, particularly the supermassive black holes (SMBHs) at the centers of galaxies. Numerous authors have used the Bondi formula to estimate the rate at which SMBHs accrete and found that it substantially overestimates the accretion rate (Di Matteo et al. 2001). Proga & Begelman (2003) have argued that rotation may explain the difference between accretion rates estimated from observations and those predicted by the Bondi rate. A third area of application is in accretion rates onto compact objects. Perna et al. (2003) suggest that a combination of rotation and magnetic fields leads to lower accretion rates onto isolated neutron stars than one would estimate using the Bondi formula. They argue that this lowered accretion rate accounts for the unexpectedly small number of isolated neutron stars that have been detected.

Previous authors have considered the problem of hydrodynamic accretion with nonzero vorticity, both analytically (Sparke & Shu 1980; Sparke 1982; Abramowicz & Zurek 1981) and numerically (Fryxell & Taam 1988; Ruffert et al. 1997, Ruffert 1999; Igumenshchev & Abramowicz 2000; Igumenshchev et al. 2000; Proga & Begelman 2003). Abramowicz & Zurek (1981) analytically treated accretion of gas with nonzero angular momentum onto a black hole. They found that for very low angular momentum the flow pattern is similar to Bondi accretion; the flow is quasi-spherical, it becomes sonic at a radius much larger than the Schwarzschild radius, and the accretion rate is comparable to the Bondi rate. For high angular momentum, the gas forms a disk and the sonic radius in the equatorial plane

becomes only a factor of a few times the Schwarzschild radius. The accretion rate is substantially below the Bondi rate. Proga & Begelman (2003) performed two-dimensional axisymmetric simulations of the accretion of slowly rotating gas onto a black hole. They find three regimes of accretion. For sufficiently low total angular momentum, the flow is Bondi-like, similar to the pattern Abramowicz & Zurek (1981) predicted. For intermediate total angular momentum, the highest angular momentum gas that cannot accrete forms a dense torus about the black hole. The torus blocks off accretion except through a thin funnel along the poles, reducing the accretion rate to a value roughly independent of the total angular momentum. Finally, for even higher total angular momentum, a centrifugal barrier, coupled with the dense torus, further reduces the accretion rate.

Our goal in this paper is to unify this work by describing the accretion process using a one-parameter family similar to the Bondi-Hoyle-Lyttleton treatment and to give an analogous formula for the accretion rate as a function of this parameter. We do this by using a combination of three-dimensional simulations and analytic treatment. In these two important respects, our work is more complete than previous work. In § 2 we give an analytic analysis of the problem and present our approximate formula. In § 3 we describe the computational methodology we use in our simulations, and in § 4 we compare the results of our simulations to the analytic theory we put forth. We summarize our conclusions in § 5.

2. ANALYTIC TREATMENT

We consider a point particle accreting in a medium with non-zero vorticity. The simplest case of this, which we treat here, is a medium with constant density and vorticity far from the particle, and where the gas has no net velocity of relative to the particle. Thus, we consider a particle at the origin of our coordinate system, surrounded by a gas whose velocity far from the particle is

$$\boldsymbol{v}_\infty = \omega_* c_\infty \frac{y}{r_B} \hat{x}, \qquad (2)$$

where $r_B \equiv GM/c_\infty^2$ is the standard Bondi radius, M is the mass of the particle, c_∞ is the sound speed of the gas at infinity, and y is the y-coordinate. The factor ω_* is a dimensionless number that we call the vorticity parameter, since the vorticity of the velocity field is $-\omega_* c_\infty / r_B \hat{z}$, independent of position.

The significance of ω_* is clear: $\omega_* = 1$ corresponds to the case where gas with an impact parameter $y = r_B$ is traveling at the sound speed at infinity. The Keplerian velocity at a distance of r_B from the central object is

$$v_K(r_B) = \sqrt{\frac{GM}{r_B}} = c_\infty. \qquad (3)$$

Thus, for $\omega_* = 1$, gas whose impact parameter is r_B is traveling at the Keplerian velocity for that impact parameter. Since $v_K \propto r^{-1/2}$, while for our initial velocity field $v_\infty \propto y$, gas with smaller impact parameters is sub-Keplerian, while gas with larger impact parameters is super-Keplerian. For $\omega_* < 1$, the transition from sub- to super-Keplerian v_∞ occurs at impact parameters larger than r_B; for $\omega_* > 1$, the transition occurs at impact parameters smaller than r_B. Because the Bondi radius is the distance at which gas comes within the gravitational sphere of influence of the central particle, provided its kinetic energy at infinity is small, we should expect a transition in behavior at $\omega_* \approx 1$.

We note that previous authors (e.g., Abramowicz & Zurek 1981; Proga & Begelman 2003) have usually parameterized their flows in terms of specific angular momentum rather than vorticity, as we do here. The choice of parameterization is somewhat a matter of taste. Specific angular momentum has the advantage of yielding a circularization radius for the flow that depends only on the specific angular momentum, simplifying the analysis. On the other hand, the choice of vorticity enables us to invoke the Kelvin circulation theorem in our analysis, which we find helpful. In addition, since specific angular momentum is a function of accretor position, and gas farther than r_B from an accretor is unaware of its presence, arranging a flow with constant specific angular momentum requires an unlikely coincidence. It is more natural to characterize a flow by its velocity gradient, hence its vorticity, which is independent of accretor position. Regardless of the choice of parameter, however, it is possible to make an approximate translation of the formulae we derive based on ω_* to ones in terms of the specific angular momentum. For the initial conditions we are considering, the specific angular momentum of a gas parcel with impact parameter y is

$$l_\infty = y v_\infty = \omega_* c_s \frac{y^2}{r_B}. \qquad (4)$$

In the artificial case of a flow with constant specific angular momentum rather than constant vorticity, the equivalent value of ω_* should be determined roughly by the value of the vorticity at the Bondi radius. Thus, as an approximate conversion we suggest $\omega_* = l_\infty / (c_s r_B)$.

Before moving on to analyze the behavior of accretion as a function of ω_*, we consider briefly the question of the gas equation of state. We choose to restrict ourselves to considering an isothermal gas, and we denote the constant sound speed as c_s. This is physically appropriate for the star formation context: radiative energy transport in the dense molecular gas from which stars form is capable of eliminating any temperature variations on times small compared to the mechanical timescales in the gas (Vázquez-Semadeni et al. 2000). In the context of SMBHs and compact objects, the thermodynamics is more complicated, as the gas can range from isothermal to adiabatic depending on the efficiency of radiative energy transport. However, based on prior simulation work with Bondi accretion (Ruffert 1994; Ruffert & Arnett 1994) and accretion with shear (Ruffert et al. 1997), we do not believe that changes in the equation of state will change either the flow pattern or the accretion rate by more than a factor of order unity.

2.1. *Very Small* ω_*

Abramowicz & Zurek (1981) performed the first detailed analysis of the cases of small and very small ω_* (which we define below), which we review and extend. We can distinguish two regimes that occur for $\omega_* \ll 1$, depending on the physical dimensions of the accreting object. In the absence of viscosity or other mechanisms of angular momentum transport, a parcel of gas has constant specific angular momentum l_∞ as it falls toward the accretor. The orbit of the gas parcel changes from predominantly radial to predominantly tangential at a characteristic circularization radius, where the parcel's velocity is roughly the Keplerian velocity. The specific angular momentum of a parcel of gas in Keplerian rotation at a distance r from the central object is

$$l_K(r) = r v_K(r) = \sqrt{GMr}, \qquad (5)$$

and the circularization radius is therefore determined by the condition $l_\infty = l_K(r_{circ})$. Equating relations (4) and (5), a gas parcel at initial impact parameter y has a circularization radius

$$r_{circ} = \omega_*^2 \frac{y^4}{r_B^3}. \tag{6}$$

If the circularization radius for a given parcel of gas is small compared to the radius of the accretor, r_A, then that gas will reach the surface of the accretor traveling in a predominantly radial orbit. Its angular momentum, and its vorticity, will therefore be deposited in the central object and will not otherwise affect the flow pattern, leading to an accretion rate approximately equal to the Bondi rate.

In the case of small vorticity, where the velocity of the gas at infinity is small compared to the Keplerian velocity, gas begins to feel the influence of the accretor at a characteristic radius of r_B. We can therefore distinguish our two regimes based on the relative sizes of $r_{circ}(r_B)$ and r_A. If $r_{circ}(r_B) < r_A$, then we are in the case analogous to that of a small circularization radius in a flow with constant specific angular momentum: the gas that reaches the accretor will be on primarily radial orbits, and the accretion rate should be the Bondi rate. The condition for this to occur is

$$\omega_* < \omega_{crit} \equiv \sqrt{\frac{r_A}{r_B}}. \tag{7}$$

We term the case $\omega_* < \omega_{crit}$ "very small ω_*." To get a sense of values of ω_{crit} in typical cases, consider some of the applications we discussed in § 1. In a star-forming region, a typical accretor mass is $M \sim M_\odot$ and a typical sound speed is $c_s \sim 0.2$ km s^{-1}, giving a Bondi radius of $r_B \sim 0.1$ pc. A typical protostellar radius is $r_A \sim 10^{12}$ cm, so $\omega_{crit} \sim 10^{-3}$. For the SMBH at the center of the Milky Way, $M \approx 3.7 \times 10^6 \, M_\odot$ for the standard distance estimate (Ghez 2004). The temperature is not constant and depends on the details of radiative processes, but a reasonable estimate for gas far from the black hole is $\sim 10^7$ K (Melia 1994), giving $c_\infty \sim$ few $\times 10^7$ cm s^{-1} and $r_B \sim 0.1$ pc. The accretor radius is the Schwarzschild radius $r_A = 2GM/c^2 \sim 10^{12}$ cm, so again $\omega_{crit} \sim 10^{-3}$.

Note that this condition $\omega_* \lesssim \omega_{crit}$ for Bondi-like accretion is roughly equivalent to the conditions of Abramowicz & Zurek (1981) and Proga & Begelman (2003) on the specific angular momentum when the accreting object is a nonrotating black hole. In that case, the accretor radius is the Schwarzschild radius, $r_A = 2GM/c^2$, so $\omega_{crit} = (2c_s/c)^{1/2}$, and the specific angular momentum of gas with impact parameter $y = r_B$ is

$$l_\infty(r_B) = \omega_{crit} c_s r_B = \sqrt{2} r_A c. \tag{8}$$

In their analytical treatment, Abramowicz & Zurek (1981) estimate that the critical specific angular momentum for Bondi-like accretion $l_\infty = 2r_A c$; however, the exact critical value will depend on the details of how the accretion flow joins onto the central object.

2.2. Small ω_*

If the vorticity is larger than ω_{crit}, but still small compared to unity, then gas circularizes before it reaches the accretor. The accretor is effectively a point particle and cannot absorb angular momentum or vorticity from the flow. In this case, Proga & Begelman (2003) have found in their simulations that gas with

too much angular momentum to accrete builds up into a torus around the accretor. This thick torus inhibits accretion by blocking off a large part of the solid angle through which streamlines could otherwise reach the accretor.

We can explain the growth of the torus by making a useful analogy to magnetohydrodynamics. The flow at infinity contains a constant vorticity. In regions of the flow that are nonviscous, the Kelvin circulation theorem requires that the vorticity contained in an area element of the fluid is constant. This is analogous to flux freezing in a magnetic medium. The accretor's gravity drags lines of vorticity in toward the accreting particle. Near the particle, where viscosity may become significant (e.g., due to magnetorotational instability in the accretion disk), gas can slip through the vortex lines and reach the accreting object. However, as long as the region of significant viscosity is confined near the accretor, the vortex lines cannot escape. As accretion drags gas inward, vortex lines build up near the accretor, just as magnetic flux would build up in a magnetic flow.

The effect of this vorticity buildup is to increase the rotational velocity in the gas. Consider a circular curve C of radius r_C in the x-y plane, centered at the origin. The circulation around curve C is the line integral of the velocity,

$$\Gamma = \oint_C \boldsymbol{v} \cdot \boldsymbol{dl} = r_C \int v_\phi d\phi, \tag{9}$$

and by Stokes' theorem

$$\Gamma = \int_A \boldsymbol{\omega} \cdot \hat{z} \, dA, \tag{10}$$

where $\boldsymbol{\omega}$ is the vector vorticity at any point in the flow and A is the area inside curve C. As a reference state, consider a velocity field with $\boldsymbol{v} = \boldsymbol{v}_\infty$ everywhere. The accretion process increases vorticity within the curve relative to this reference state, so it must also increase Γ and hence the mean rotational velocity v_ϕ around C. Because the vorticity parameter $\omega_* < 1$, we know that initially $v_\phi < v_K$ as long as $r_C < r_B$. However, this analysis shows that v_ϕ increases with time, so eventually the rotational velocity will become comparable to the Keplerian velocity and a rotationally supported disk must form. The Keplerian velocity is supersonic for all radii smaller than r_B, and the inflow onto the disk is not purely radial, so the disk will likely develop internal shocks and a time-dependent structure.

The process of vorticity increase near the accretor cannot continue indefinitely. Eventually, inward transport of vorticity by accreting matter must be balanced by an outward flow of vorticity in gas leaving the vicinity of the accretor and escaping to infinity. The radius at which gas becomes unbound from the accretor and can start escaping is r_B, and we therefore expect that the disk will extend out to $\sim r_B$ in radius. The scale height of a thin Keplerian disk is

$$H = \frac{c_s}{\Omega} = c_s \sqrt{\frac{r^3}{GM}} = r \sqrt{\frac{r}{r_B}}, \tag{11}$$

where Ω is the angular velocity. Since the disk radius is $\sim r_B$, we expect $H \sim r_B$. Thus, the scale height is comparable to the radius and we have, rather than a disk, a thick torus. The torus may be somewhat thicker for an equation of state with ratio of specific heats γ greater than unity, because in that case the sound speed will increase inside the Bondi radius because of compressional heating. However, the compression is only of

order unity at $r \sim r_B$, so the effect of compression on the torus scale height should also be of order unity.

The circulation trapped within the torus should be

$$\Gamma \sim 2\pi r_B v_K(r_B) = 2\pi c_s r_B. \tag{12}$$

In our reference state with $\boldsymbol{v} = \boldsymbol{v}_\infty$ everywhere, the circulation is

$$\Gamma_0 = \pi r_B^2 \omega = \pi c_s r_B \omega_*, \tag{13}$$

which is clearly much smaller than the equilibrium value of Γ for $\omega_* \ll 1$. The time required for the circulation to build up to Γ is determined by the rate at which mass falling onto the accreting object carries vorticity inward. The gas within the Bondi radius reaches the central object, or the growing disk, on the Bondi timescale, $t_B \equiv r_B/c_s$. Thus, the flow replaces the gas within the Bondi radius on this timescale. Each set of "replacement" gas carries the same vorticity as the gas it is replacing and therefore increases the circulation by Γ_0. As a result, the time required for the accumulating vorticity to reach its equilibrium value is approximately

$$t_{eq} \sim \frac{\Gamma}{\Gamma_0} t_B = \frac{2}{\omega_*} t_B. \tag{14}$$

This estimate only applies for $\omega_* \lesssim 1$, when accumulation of circulation is the key factor in setting the final accretion rate.

We can roughly estimate the amount by which the accretion rate will be reduced by the presence of the torus once the flow reaches equilibrium. The torus reduces accretion by blocking off the solid angle through which material could otherwise accrete. If the torus extends out to r_B, and its height is roughly r_B as well, it blocks all angles in the range $\pi/4 < \theta < 3\pi/4$. If the reduction in accretion rate is proportional to the fraction of solid angle blocked, then the accretion rate for this case should be reduced to $\sim 30\%$ of the Bondi rate, $\dot{M}_B$, given by equation (1) for $\mathcal{M} = 0$.

It is important to note that the equilibrium state we describe here does not depend on the value of ω_*, as long as $\omega_{crit} < \omega_* \ll 1$. The equilibrium radius of the torus depends only on the maximum vorticity that can accumulate near the accretor before the velocity becomes comparable to the Kepler velocity and halts infall in the disk. Thus, the equilibrium radius of the torus is $\sim r_B$ independent of ω_*, and the scale height and accretion rate are also $H \sim r_B$ and $\dot{M} \sim 0.3\dot{M}_B$, respectively. Different values of ω_* only mean that vorticity builds up more or less slowly, and thus that there is a longer or shorter initial transient.

2.3. Large ω_*

The final case to consider is $\omega_* \gtrsim 1$. In this regime, the velocity of the gas at the Bondi radius is comparable to or larger than the Keplerian velocity. To derive an approximate accretion rate, we adopt an *Ansatz* from Bondi-Hoyle accretion.

Regardless of its velocity, gas at infinity initially has a positive total energy. Its potential energy is zero, and it has nonzero internal energy. In order to become bound and accrete onto the point mass, the gas must lose its energy by shocking. If gas does shock, it is likely to accrete. Since the flow at infinity is laminar, shocks will only occur for those streamlines that are bent significantly by the gravity of the accreting particle. To determine if a straight streamline is susceptible to bending, we can compare the velocity of gas on that streamline (adding both bulk and thermal velocity) to the maximum value of the escape velocity

along that streamline. If the peak escape velocity is larger, then the streamline will bend and is likely to terminate in a shock. Suppose the gas at infinity is traveling in the x-direction, and consider a streamline that begins at x, y, z coordinates $(\pm\infty, y, z)$. The streamline will bend significantly and pass through a shock if

$$\frac{2GM}{\sqrt{y^2 + z^2}} > v_\infty(y,z)^2 + c_s^2. \tag{15}$$

In the Bondi-Hoyle case, $v_\infty = \mathcal{M}c_s$ independent of y and z. Thus, equation (15) reduces to

$$\sqrt{y^2 + z^2} < \frac{2GM}{c_s^2(1 + \mathcal{M}^2)} \equiv 2r_{BH}, \tag{16}$$

where we have used the standard definition for the Bondi-Hoyle radius.

If we make the assumption that all parcels of gas traveling on streamlines that bend significantly go through shocks and that all gas that shocks loses enough energy to become bound and eventually reach the accretor, then the rate at which mass accretes onto the particle is equal to the rate at which gas from infinity begins traveling on streamlines that meet condition (15). We can therefore define an area A in the plane at infinity that satisfies equation (15) and approximate the accretion rate by

$$\dot{M} \approx \int_A \rho_\infty \sqrt{v_\infty(y,z)^2 + c_s^2} \, dy \, dz, \tag{17}$$

where ρ_∞ is the density of the gas at infinity and we have again added the bulk and thermal velocities of the gas in quadrature. For the Bondi-Hoyle case, A is simply a circle of radius of radius $2r_{BH}$ and v_∞ is a constant, so the integral is trivial. Evaluating it gives

$$\dot{M}_{BH} \approx 4\pi r_{BH}^2 \rho_\infty c_s \sqrt{1 + \mathcal{M}^2} = 4\pi\rho_\infty \frac{(GM)^2}{c_s^3(1 + \mathcal{M}^2)^{3/2}}, \tag{18}$$

which is just the Bondi-Hoyle formula (eq. [1]) up to factors of order unity.

Because this *Ansatz* allows us to reproduce the Bondi-Hoyle formula, we apply it to predict the case of accretion with vorticity. In this case, $v_\infty = \omega_* c_s y/r_B$, so equation (15) becomes

$$\frac{2GM}{\sqrt{y^2 + z^2}} > \left(\omega_* \frac{c_s}{r_B}\right)^2 y^2 + c_s^2. \tag{19}$$

With the convenient change of variable $y' = y/r_B$ and $z' = z/r_B$, this becomes

$$2 > \left(y'^2 + z'^2\right)^{1/2}\left(1 + \omega_*^2 y'^2\right). \tag{20}$$

We can solve equation (20) for z' to find the function $Z'(y', \omega_*)$ that defines the boundary:

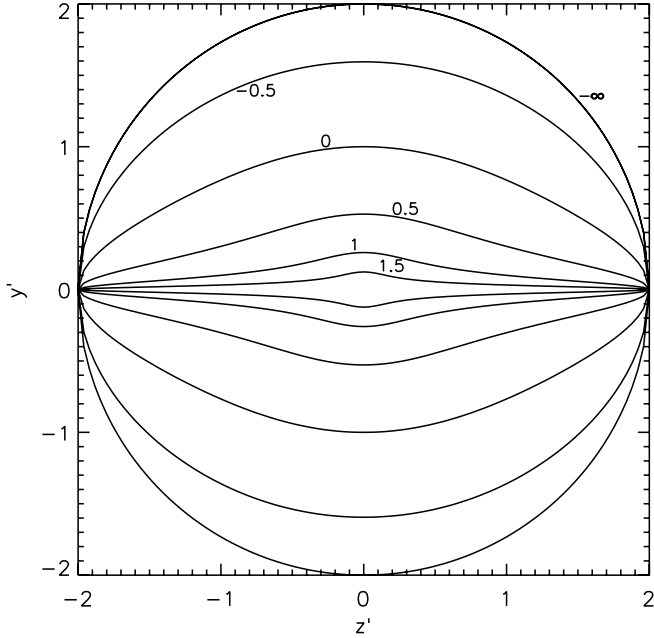$$Z'(y', \omega_*) = \frac{\sqrt{4 - y'^2(1 + \omega_*^2 y'^2)^2}}{1 + \omega_*^2 y'^2}. \tag{21}$$

FIG. 1.—Plot shows the area $A(\omega_*)$, as defined by eq. (21), for different values of ω_*. The numbers indicate the value of $\log\omega_*$ for each curve.

We refer to region of the y-z plane bounded by $\pm Z'(y', \omega_*)$ as $A(\omega_*)$. The maximum value of y' on the boundary of $A(\omega_*)$ occurs for $z' = 0$ and is

$$y'_{\max}(\omega_*) = \frac{3^{1/3}\left(9\omega_* + \sqrt{3 + 81\omega_*^2}\right)^{2/3} - 3^{2/3}}{3\omega_*\left(9\omega_* + \sqrt{3 + 81\omega_*^2}\right)^{1/3}}. \quad (22)$$

Figure 1 shows the boundary of $A(\omega_*)$ as a function of ω_*.

The approximate accretion rate is

$$\dot{M}(\omega_*) \approx r_{\rm B}^2 \rho_\infty c_s \int_{A(\omega_*)} \sqrt{1 + \omega_*^2 y'^2}\, dy'\, dz' \quad (23)$$

$$\equiv 4\pi r_{\rm B}^2 \rho_\infty c_s f(\omega_*), \quad (24)$$

where we have defined the numerical factor

$$f(\omega_*) = \frac{1}{4\pi} \int_{A(\omega_*)} \sqrt{1 + \omega_*^2 y'^2}\, dy'\, dz' \quad (25)$$

$$= \frac{1}{\pi} \int_0^{y'_{\max}(\omega_*)} \sqrt{1 + \omega_*^2 y'^2} \int_0^{Z'(y', \omega_*)} dz'\, dy' \quad (26)$$

$$= \frac{1}{\pi} \int_0^{y'_{\max}(\omega_*)} \sqrt{\frac{4 - y'^2(1 + \omega_*^2 y'^2)^2}{1 + \omega_*^2 y'^2}}\, dy'. \quad (27)$$

The integral is straightforward to evaluate numerically, and we plot the result in Figure 2. We can also obtain an approximation for $f(\omega_*)$ in the limit $\omega_* \to \infty$. We show in the Appendix that in the limit $\omega_* \gg 1$ we can approximate $f(\omega_*)$ by

$$f(\omega_*) \approx \frac{2}{3\pi\omega_*} \ln(16\omega_*). \quad (28)$$

We also show this approximation in Figure 2.

We must make one further modification to our estimated accretion rate. In the limit $\omega_* \to 0$, $f(\omega_*) \to 1$ and equation (24) reduces to approximately $\dot{M}_{\rm B}$. Thus, this approximation smoothly
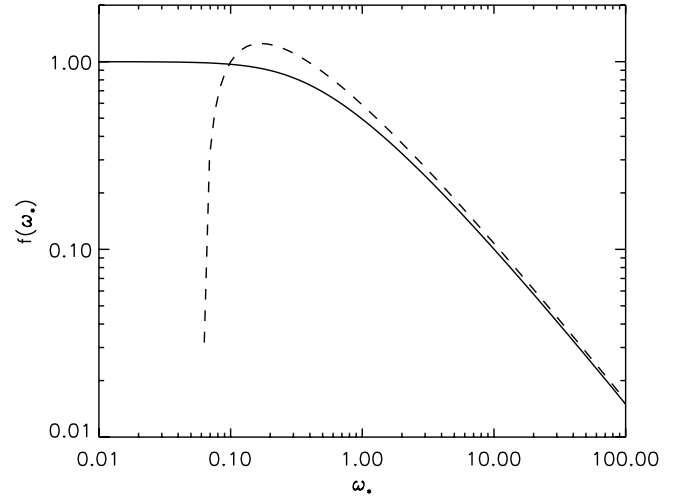

FIG. 2.—Solid line shows $f(\omega_*)$, as defined by eq. (27). The dashed line shows the large-ω_* approximation given by eq. (28).

interpolates between the cases $\omega_* \ll 1$ and $\omega_* \gtrsim 1$. However, we have already seen that even in the case $\omega_* \ll 1$ the accretion rate can be substantially below the Bondi rate, since the accumulation of circulation leads to the formation of a thick torus that blocks streamlines from reaching the accretor. The same phenomenon should happen with $\omega_* \gtrsim 1$. Circulation will still accumulate near the accretor. The shape of the torus should be the same as in the $\omega_* \ll 1$ case, because that is set just by the physics of disks. We therefore reduce our estimated accretion rate (eq. [24]) by a constant factor so that it matches our estimate of $0.3\dot{M}_{\rm B}$ for the case $\omega_{\rm crit} < \omega_* \ll 1$. The required factor is 0.34; it is not exactly 0.3 because equation (24) for $\omega_* \ll 1$ differs from the Bondi rate by a small factor.

With this modification in place, equation (24) should give a good approximation of the accretion rate for all $\omega_* > \omega_{\rm crit}$. Our final estimate for the accretion rate by a flow with vorticity ω_* at infinity is

$$\dot{M}(\omega_*) \approx 4\pi\rho_\infty \frac{(GM)^2}{c_s^3} \times \begin{cases} \exp(1.5)/4 & \omega_* < \omega_{\rm crit}, \\ 0.34 f(\omega_*) & \omega_* > \omega_{\rm crit}. \end{cases} \quad (29)$$

In § 5 we give a more accurate approximation that is calibrated by our simulations.

3. COMPUTATIONAL METHODOLOGY

To test the theory presented in the previous section, we ran a series of simulations. In this section, we describe the simulation methodology, and in the next section, we compare the simulation results to our theory.

3.1. Code

The calculations in this paper use our three-dimensional adaptive mesh refinement (AMR) code to solve the Euler equations of compressible gasdynamics,

$$\frac{\partial\rho}{\partial t} + \nabla\cdot(\rho\boldsymbol{v}) = 0, \quad (30)$$

$$\frac{\partial}{\partial t}(\rho\boldsymbol{v}) + \nabla\cdot(\rho\boldsymbol{vv}) = -\nabla P - \rho\nabla\phi, \quad (31)$$

$$\frac{\partial}{\partial t}(\rho e) + \nabla\cdot[(\rho e + P)\boldsymbol{v}] = \rho\boldsymbol{v}\cdot\nabla\phi, \quad (32)$$

<div align="center">

TABLE 1

Simulation Parameters and Results

</div>

ω_* (1)	$\Delta x_{\min}/r_B$ (2)	y_{range}/r_B (3)	t_{run}/t_B (4)	t_{eq}/t_B (5)	$\overline{\dot{M}/\dot{M}_B}$ (6)	$\sigma_{\dot{M}}$ (7)	$\overline{\Gamma}_*$ (8)
0.............................	0.025	[−40, 40]	77	7	0.99	0.007	2.3×10^{-4}
10^{-2}.........................	0.025	[−40, 40]	200	100	0.36	0.099	0.49
$10^{-1.5}$......................	0.025	[−40, 40]	120	30	0.31	0.099	0.56
10^{-1}.........................	0.025	[−40, 40]	50	15	0.25	0.061	0.65
$10^{-0.5}$......................	0.025	[−40, 40]	63	30	0.34	0.15	0.38
10^{0}	0.025	[−40, 40]	19	12	0.22	0.10	0.42
$10^{0.5}$	0.025	[−12.5, 12.5]	18	4	0.088	0.22	0.75
10^{1}..........................	0.0061	[−6.3, 6.3]	4.3	1.5	0.048	0.19	6.7
$10^{1.5}$........................	0.0061	[−12.5, 12.5]	0.96	0.7	0.018	0.037	29.2

Notes.—Col. (1): Vorticity parameter. Col. (2): Grid spacing in Bondi radii. Col. (3): Size of simulation region in the y-direction. Col. (4): Run duration in Bondi times. Col. (5): Approximate time the accretion rate reaches equilibrium, in Bondi times. Col. (6): Mean accretion rate, in units of the Bondi rate. Col. (7): Standard deviation in accretion rate, as a fraction of the mean accretion rate. Col. (8): Mean dimensionless circulation.

where ρ is the density, $\boldsymbol{v}$ is the vector velocity, P is the thermal pressure (equal to ρc_s^2 since we adopt an isothermal equation of state), e is the total nongravitational energy per unit mass, and ϕ is the gravitational potential. The code solves these equations using a conservative high-order Godunov scheme with an optimized approximate Riemann solver (Toro 1997). The algorithm is second-order accurate in both space and time for smooth flows, and it provides robust treatment of shocks and discontinuities. Although the code is capable of solving the Poisson equation for the gravitational field ϕ of the gas based on the density distribution, in this work we neglect the gas self-gravity and include only the gravitational force of the central object. The potential is therefore

$$\phi = \frac{GM}{r}, \qquad (33)$$

where M is the mass of the central object and r is the distance from it. We do not adopt the Paczyński & Wiita (1980) potential frequently used for simulations involving black holes because we do not wish to limit ourselves to the case of black holes, and because even in the black hole case, we are interested in the regime where the Schwarzschild radius is extremely small on scales of the grid, so that general relativistic effects are not important.

Our code operates within the AMR framework (Berger & Oliger 1984; Berger & Collela 1989; Bell et al. 1994) and is described in detail in Truelove et al. (1998) and Klein (1999). We discretize the problem domain onto a base, coarse level, denoted level 0. We dynamically create finer levels, numbered $1, 2, \ldots n$, recursively nested within one another. To take a time step, one advances level 0 through a single time step Δt_0, and then advances each subsequent level for the same amount of time. Each level has its own time step, and in general $\Delta t_{l+1} < \Delta t_l$, so after advancing level 0 we must advance level 1 through several steps of size Δt_1, until it has advanced a total time Δt_0 as well. In all the simulations we present in this paper, we chose cell spacings such that $\Delta t_l = 2\Delta t_{l+1}$, and thus we take two time steps on level 1 for each time step on level 0. (We find that refining by factors of 2 gives better accuracy in the solution than using a larger refinement factor.) After each level 0 time step, we apply a synchronization procedure to guarantee conservation of mass, momentum, and energy across the boundary between levels 0 and 1. However, each time we advance level 1

through time Δt_1, we must advance level 2 through two steps of size Δt_2, and so forth to the finest level present.

On the finest level of refinement, we represent the central, accreting object with a sink particle (Krumholz et al. 2004). One noteworthy feature of our sink particle, which we discuss further in § 3.3, is that the sink particle does not accrete any angular momentum from the gas in the computational grid. This is in contrast the sink methodologies used by previous authors (e.g., Ruffert et al. 1997; Proga & Begelman 2003), where the sink could accrete angular momentum as well as mass. Our approach is appropriate for $\omega_* \gg \omega_{crit}$, which is the case on which we focus.

3.2. Initial and Boundary Conditions

For each run, we place a sink particle at the origin of an initially uniform gas. The gas has an initial velocity field

$$\boldsymbol{v}_0 = \omega_* c_s \frac{y}{r_B} \hat{x}, \qquad (34)$$

where we use different values of ω_* in different runs. Table 1 summarizes the values of ω_* that we simulated. Our computational domain extends from $-100 r_B$ to $100 r_B$ in the x- and z-directions. In the y-direction, we also used a range of $-100 r_B$ to $100 r_B$ for smaller values of ω_*. For larger values of ω_*, however, the large velocities that occur at large values of y produce very small time steps that make the computation prohibitively expensive. We therefore use a smaller domain in the y-direction, as we indicate in Table 1; in every case, however, we chose our domain to extend to values of y such that $v_0(y_{max}) \gg v_{escape}(y_{max})$.

We used inflow/outflow boundary conditions in the x-direction and symmetry in the y- and z-directions. However, for all our runs the boundary is sufficiently far away from the central object that, within the duration of the run, no sound waves can propagate from the central object to the boundary and back. Our lowest resolution runs have $\Delta x_{min} < r_B/40$, which we use for smaller values of ω_*. For larger values of ω_*, we use $\Delta x_{min} < r_B/160$. We set up our adaptive grids such that, at any radius r, the local grid resolution is $\Delta x \leq \max(r/20, \Delta x_{min})$.

3.3. The Sink Particle Method and Very Small Vorticity

As Table 1 indicates, we vary ω_* from 10^{-2} to $10^{1.5}$, thereby thoroughly exploring the small-ω_* and large-ω_* regimes.

However, none of our work explores the very small ω_* regime. This is for two reasons, one physical and one technical. In order to explore the very small ω_* case, one must use either an unphysically small value of ω_* or an unphysically large accretor radius, leading to an unrealistically large ω_{crit}. As we have shown in § 2.1, for typical astrophysical situations in which accretion with vorticity is important, $\omega_{crit} \sim 10^{-3}$. This is a truly tiny amount of vorticity, corresponding to a shear of one-thousandth of the sound speed at one Bondi radius. In the case of a protostar in a molecular clump, this corresponds to a velocity gradient of no more than ~ 10 cm s^{-1} over a distance of ~ 0.1 pc; for the galactic center, it corresponds to a gradient of $\sim 10^4$ cm s^{-1} over a distance of ~ 0.1 pc. It is difficult to see how to produce such an irrotational flow field, and thus the very small ω_* case is not relevant for the applications with which we are concerned.

The technical reason why we do not treat the very small ω_* case is that our sink particle method is constructed to exactly conserve total angular momentum during the accretion process. (For details, see Krumholz et al. 2004.) Transfer of vorticity from the flow to the accretor is the distinguishing characteristic of flow with $\omega_* < \omega_{crit}$. However, since our sink particle does not change the angular momentum of the flow field, it actually increases vorticity by removing mass while leaving angular momentum. Our code does dissipate vorticity via numerical viscosity, as we discuss in more detail in § 4.4 on convergence testing. However, this effect is small except in the inner few zones. On balance, we consider this approach more realistic than the standard technique of allowing any angular momentum that enters a chosen accretion region to accrete. In reality, a small accretor should absorb negligible angular momentum from the flow on scales much larger than the accretor radius. In real accretion disks, viscosity acts to transfer mass inward and angular momentum outward. This is exactly the approximation we adopt in our sink particle method: mass travels inward, angular momentum does not. While ideally one would follow the flow down to the true physical surface of the accretor, this is computationally infeasible in more than one dimension, even with AMR. Our sink particle method provides a more realistic approximation of the behavior of an accretion disk than would allowing angular momentum to accrete.

4. SIMULATION RESULTS

4.1. Density and Velocity Fields

In each of the simulations, the flow went through a transient and then settled down into a quasi-equilibrium state. The time required to reach equilibrium increased with decreasing ω_*, ranging from $\sim 100 t_B$ for $\omega_* = 10^{-2}$ to $\sim t_B$ for $\omega_* \gtrsim 1$, where $t_B \equiv r_B/c_s$ is the Bondi time. In the equilibrium configuration, all the runs except $\omega_* = 0$ built up dense material around the accretor. The material was not in a symmetric disk, but rather in a pinwheel shape. The velocity patterns associated with these pinwheels generally involved matter flowing in from the z-direction through an accretion funnel and either circulating or outflowing in the x-y plane. This overall morphology agrees well with the results of Proga & Begelman (2003). Figures 3, 4, and 5 illustrate the morphology for $\omega_* = 10^{-2}$, 1, and $10^{1.5}$.

A comparison of runs at different ω_*-values shows several clear trends. First, the accumulated pinwheel of matter is much smaller at large ω_* than at small ω_*. For $\omega_* \lesssim 1$, the accumulated matter extends out to $\sim r_B/2$, while for $\omega_* \gg 1$ it is well inside the Bondi radius and is less massive. The size of the pinwheel changes only slightly with ω_* for $\omega_* \lesssim 1$, but shrinks dramatically for $\omega_* \gtrsim 1$. Our theoretical description of the torus we
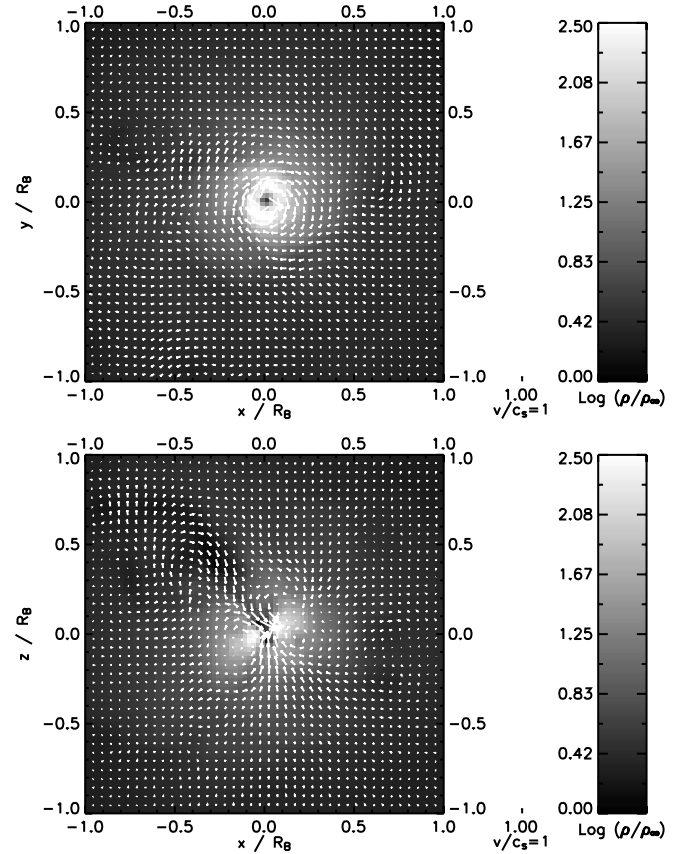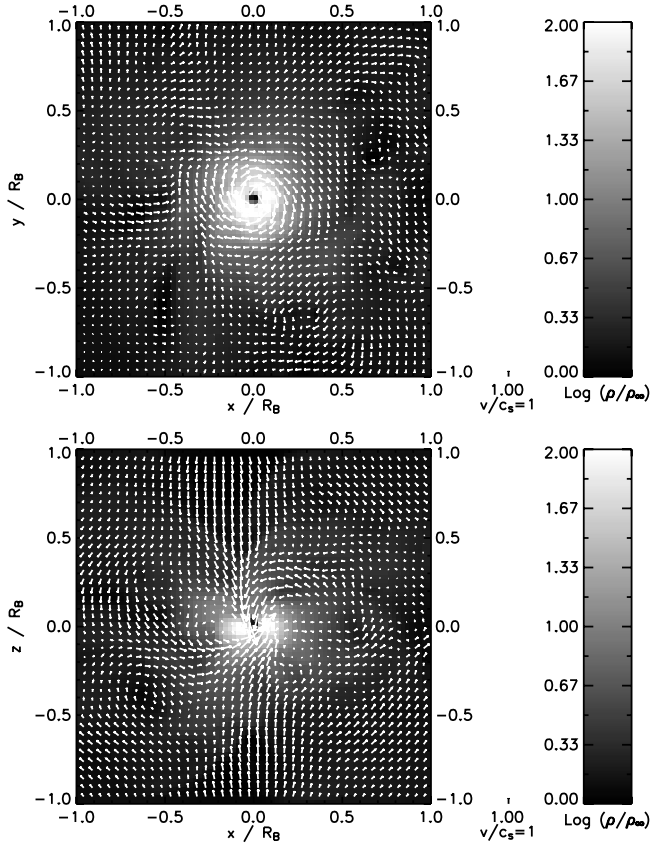

Fig. 3.—Plots show slices through the origin in the x-y and x-z planes for the $\omega_* = 10^{-2}$ run. The gray scale indicates log density, and the arrows indicate velocity. Note the differences in scale from Figs. 4 and 5. [*See the electronic edition of the Journal for a color version of this figure.*]

expect for small ω_* appears to be roughly correct: a torus of material accumulates that extends out to $\sim r_B$ and has a height comparable to its radius. The tori are chaotic and time variable. For larger ω_*, the pinwheels are more regular and less chaotic and are accompanied by leading and trailing shocks. The shocks are moderately strong, with Mach numbers $\sim 2-3$.

For $\omega_* \lesssim 1$, we do not find that the torus has constant specific angular momentum, as Proga & Begelman (2003) did. In our tori, the specific angular momentum of the gas varies by orders of magnitude. It is unclear whether this difference in results is due to different initial conditions or due to the fact that our simulations are three-dimensional, whereas theirs were two-dimensional. However, we agree with Proga & Begelman (2003) that the size and shape of the torus is largely independent of ω_* (or the initial specific angular momentum l), and that its equilibrium structure arises because of the accumulation of material with too much vorticity (or l) to accrete. As Figures 3 and 4 show, accretion occurs only through a narrow funnel, and the (invariant) shape of the torus therefore determines the accretion rate.

4.2. Evolution of Circulation

For each run we computed the average dimensionless circulation Γ as a function of time. We define the dimensionless circulation within a circle of radius r_B in the x-y plane as

$$\Gamma_* = -\frac{1}{\pi r_B c_s} \oint_{r=r_B} \boldsymbol{v} \cdot \boldsymbol{dl}, \qquad (35)$$

Fig. 4.—Plots show slices through the origin in the *x-y* and *x-z* planes for the $\omega_* = 1$ run. The gray scale indicates log density, and the arrows indicate velocity. Note the differences in scale from Figs. 3 and 5. [*See the electronic edition of the Journal for a color version of this figure.*]

Fig. 5.—Plots show slices through the origin in the *x-y* and *x-z* planes for the $\omega_* = 10^{1.5}$ run. The gray scale indicates log density, and the arrows indicate velocity. Note the differences in scale from Figs. 3 and 4. [*See the electronic edition of the Journal for a color version of this figure.*]

where the line integral is evaluated on the circle $r = r_B$. The circulation is a measure of the amount of vorticity within one Bondi radius of the accretor. With this definition of dimensionless circulation, in the initial configuration of the velocity field the circulation is equal to the vorticity parameter, $\Gamma_* = \omega_*$. Our prediction for the equilibrium circulation for $\omega_* \lesssim 1$ is $\Gamma \sim 2\pi c_s r_B$, or $\Gamma_* \sim 2$.

We plot the circulation versus time along with the accretion rate versus time for each of our runs in Figure 6. The behavior of the circulation with time depends on the value of ω_*. For $\omega_* \lesssim 1$, the circulation starts at ω_* and gradually increases until it reaches $\sim 0.4-0.8$. Then it fluctuates around this mean. For $\omega_* = 10^{0.5}$, Γ_* decreases from its initial value until it again reaches the range $\sim 0.4-0.8$. As ω_* increases, however, Γ_* decreases less and less in the time it takes the accretion rate to reach equilibrium. The accretion rate and the circulation appear to be anticorrelated for $\omega_* \lesssim 1$ in the period before equilibration: the initial buildup of circulation takes about the same amount of time as the initial decrease in the accretion rate. This supports our hypothesis that vortex lines are acting like magnetic flux lines and inhibiting accretion.

For each run we estimate by eye the time at which the flow pattern and accretion rate reach equilibrium, and we compute the mean circulation after this time. We report the equilibration times and the mean circulations in Table 1; we plot the equilibrium value of Γ_* in Figure 7 and the equilibration time in Figure 8. As the figures show, the equilibrium value of the circulation is at most very weakly dependent on the initial vorticity for $\omega_* \lesssim 1$, varying by less than a factor of 2, while the initial vorticity varies
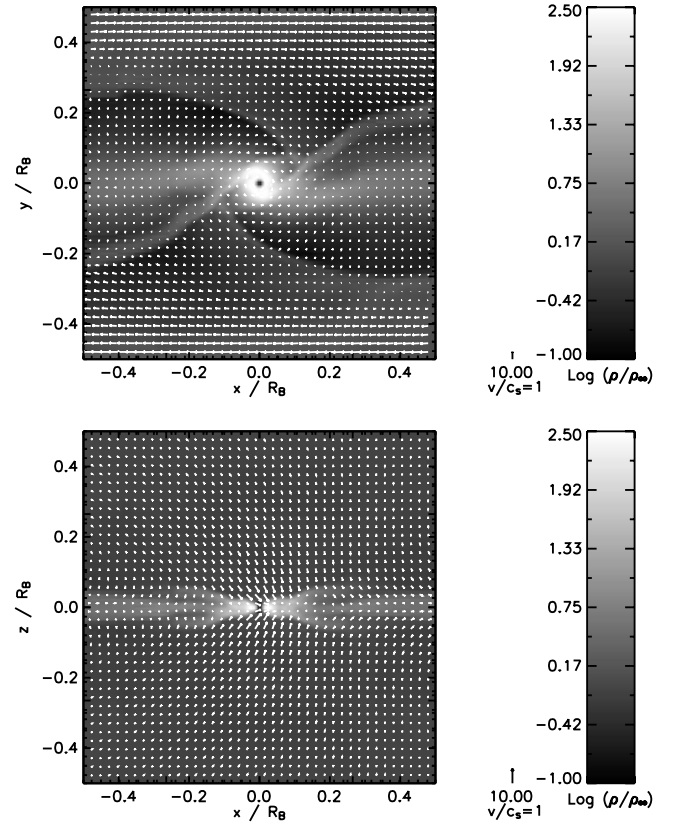
by a factor of 100. The flow pattern rearranges itself to select $\Gamma \sim 0.4-0.8$ by accumulating a dense torus of material rotating at nearly Keplerian speeds around the accretor. The equilibrium value is smaller than our prediction of $\Gamma_* \sim 2$, indicating that the rotational velocity is sub-Keplerian. This result is consistent with the morphology of the gas flow. The gas has a nonzero radial velocity and thus can be marginally bound even with tangential velocities that are sub-Keplerian. Our analytic model, because it fails to predict the chaotic nature of the flow pattern, overestimates the equilibrium value of Γ_* by a factor of ~ 4. It does, however, correctly predict that there is an equilibrium Γ_* for $\omega_* \lesssim 1$. At $\omega_* \gtrsim 1$, the pinwheel of unaccreted matter is confined closer to the accretor and is unable to affect the circulation on length scales $\sim r_B$. Thus, the circulation for larger ω_* stays constant.

The equilibration time is also roughly consistent with our prediction of $t_{eq} = 2t_B/\omega_*$ for $\omega_* \lesssim 1$. Part of the scatter of the line comes from the unavoidable subjectivity in our estimate of the equilibration time in such a chaotic flow. However, our model is clearly only approximate. While we correctly capture the trend of increasing equilibration time with decreasing ω_*, our inability to model the turbulent flow means that our prediction of the equilibration time, like our prediction of Γ_*, is accurate to at best a factor of a few.

In the plots of Γ_* and t_{eq} versus ω_* (and, as we show below, in the plot of $\dot{M}$ vs. ω_* as well), there seems to be a change in behavior between the $\omega_* = 10^{-1}$ and $\omega_* = 10^{-0.5}$ runs. Rather than smoothly interpolating between $\omega_* \ll 1$ and $\omega_* \gg 1$, the trend with ω_* appears to jump from one track to another. We cannot rule out the possibility that this is simply the result of
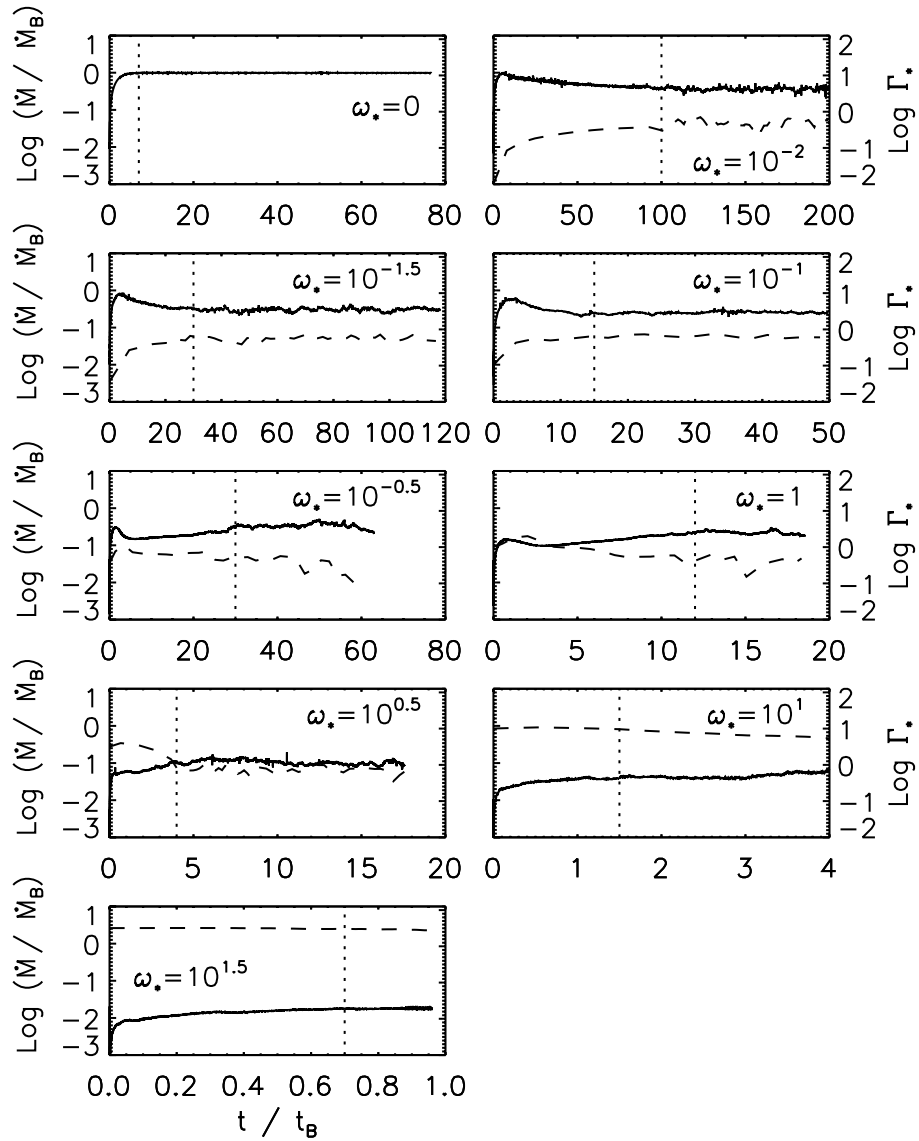
Fig. 6.—Plots show the accretion rate vs. time (*solid lines*) and circulation vs. time (*dashed lines*) for the run with the value of ω_* indicated in the panel. The dotted vertical lines indicate the time at which we conclude the system has reached equilibrium.
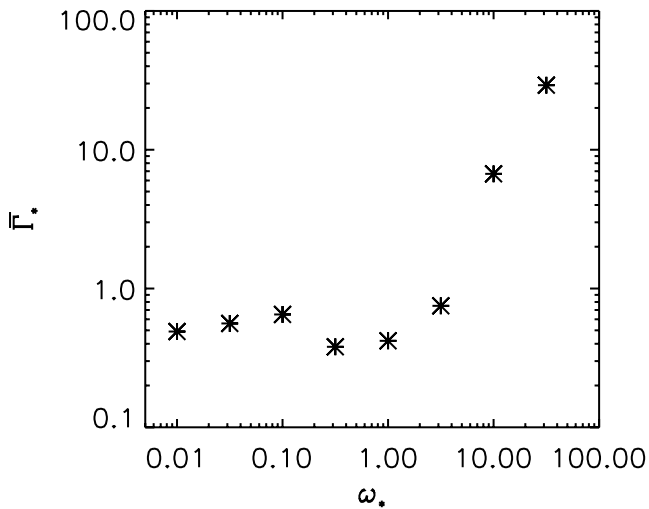

Fig. 7.—Asterisks indicate the mean value of Γ_* after equilibration for each of our runs as a function of ω_*.
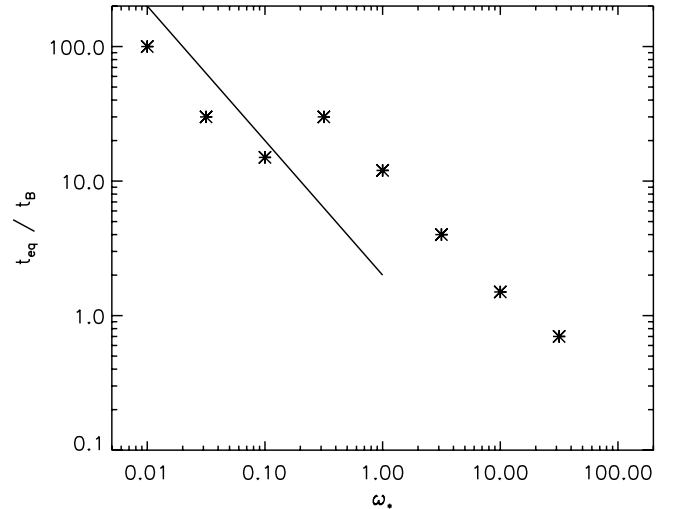
Fig. 8.—Asterisks indicate the time (in units of t_B) at which the run reaches equilibrium for each value of ω_*. The line is our prediction $t_{eq} = 2t_B/\omega_*$.
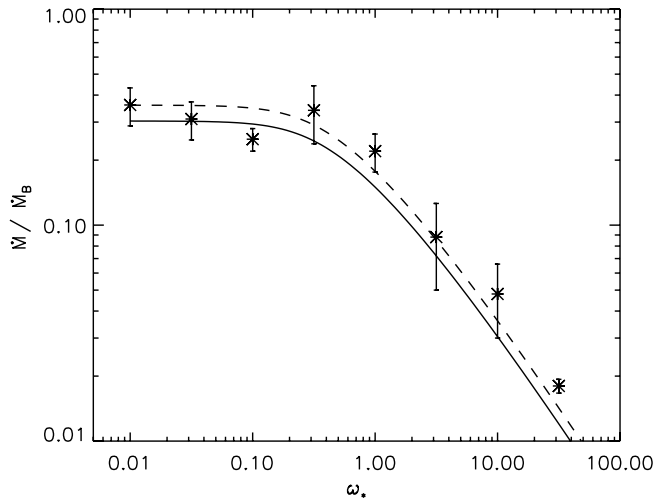
Fig. 9.—Plot shows mean accretion rate, in units of the Bondi rate, vs. ω_*. The asterisks are the simulation data, with error bars indicating 2 times the standard deviation in the accretion rate. The solid line is our theoretical prediction (eq. [29]). The dashed line is the theoretical prediction scaled by a constant factor to give the best possible fit to the simulation data.
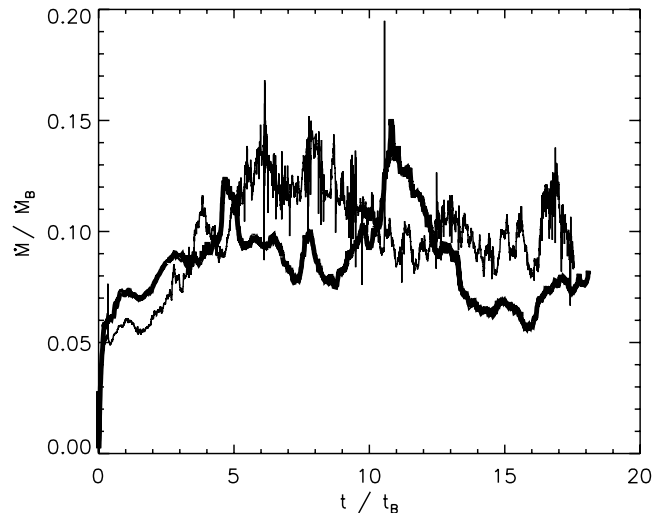

Fig. 10.—Plot shows the accretion rate vs. time for our convergence test. The thick line is the $\omega_* = 10^{0.5}$ run at a resolution of $r_B/\Delta x = 40$, and the thin line is the run at a resolution of $r_B/\Delta x = 160$.

chance and our sparse sampling of ω_*-values. Near $\omega_* = 1$, the equilibrium values of quantities such as Γ_* and t_{eq} may be fluctuating chaotically with ω_*, and the sharp jump we see from $\omega_* = 10^{-1}$ to $\omega_* = 10^{-1/2}$ may just be a fluctuation. However, it is also possible that there is a distinct regime of intermediate ω_*, as well as the small and large ω_*, and that several properties of the equilibrium flow change suddenly when one enters this new regime.

4.3. Accretion Rates and Comparison to Theory

We ran each of our simulations until the accretion rate converged to a steady state, and then we measured both the mean accretion rate and the fluctuations about the mean. Table 1 summarizes our results, and Figure 6 shows the accretion rate versus time for each run. We filter out short-timescale noise associated with the finite resolution of our simulation by only computing the standard deviation in accretion rate averaged over 16 time steps. Nonetheless, discreteness error does lead to a nonzero standard deviation even in the case $\omega_* = 0$, which is pure Bondi accretion and should have zero standard deviation. The standard deviation of 0.007% gives a lower limit on our ability to measure fluctuations in the accretion rate. Since the standard deviations we measure for other runs are significantly larger than this, they likely represent real physical time variability, not just simulation noise.

We plot the mean accretion rate as a function of ω_* in Figure 9. We also show our theoretical prediction (*solid line*), which fits the data reasonably well. To obtain a somewhat better fit, we keep the function $f(\omega_*)$ the same and do a least-squares fit to obtain a prefactor to replace 0.34 in equation (29). We find a best-fit value of 0.40. This value produces a good fit, as shown in the dashed line in Figure 9. The formula fits each of the simulation values to better than 40%. This is comparable to the accuracy of the Bondi-Hoyle formula at intermediate Mach numbers (Ruffert 1994; Ruffert & Arnett 1994).

4.4. Convergence Testing and Dependence on r_A/r_B

To test the convergence of our simulations, we repeated one of our runs at higher resolution. Perna et al. (2003) have hypothesized that the accretion rate in Bondi accretion with vorticity is

proportional to $(r_A/r_B)^p$, where p is between 0.5 and 1. Proga & Begelman (2003) saw a small dependence of the accretion rate on r_A/r_B for some of their simulations with smaller dynamic ranges, but the variation seemed to disappear in their simulations with larger dynamic ranges. In our sink particle method, the central object cannot accrete angular momentum, so in the absence of numerical viscosity, we would be in the limit $r_A/r_B \ll 1$. However, as we have noted above, numerical viscosity does set an effective minimum size for our accretor. In the inner few cells of the simulation grid, where the circles in which the gas is attempting to move are poorly resolved, our code does not perfectly conserve angular momentum or vorticity. It is difficult to determine an equivalent accretor size set by this phenomenon, but we have found that even at our lowest resolution of $r_B/\Delta x = 40$, our simulations produce disks and accumulation of circulation rather than Bondi-like flow for ω_* as small as 10^{-3}. Thus, the effective value of r_A/r_B set by our method must be $\lesssim 10^{-3}$. (Recall that typical values of r_A/r_B in astrophysical systems are closer to 10^{-6}.) Regardless of the true effective accretor radius imposed by numerical viscosity, by changing the grid size, and thus the rate of angular momentum dissipation, we are testing whether the accretion rate truly depends on r_A/r_B when $r_A/r_B \ll 1$.

To test for convergence, we reran our simulation with $\omega_* = 10^{0.5}$ at a resolution of $r_B/\Delta x = 160$, 4 times the fiducial resolution. All other aspects of the simulation were identical. We plot the accretion rate versus time for the two differently resolved versions of the run in Figure 10. As the results show, the exact shape of the accretion rate versus time graph is not the same at the different resolutions. This is to be expected in an unstable and chaotic flow. However, the overall accretion rates appear to be approximately the same. We find a mean accretion rate after equilibration of $0.088\dot{M}_B$ for the run with $r_B/\Delta x = 40$, and a mean of $0.11\dot{M}_B$ for the run with $r_B/\Delta x = 160$. The standard deviations in the accretion rates are 22% and 14%, respectively, while the difference in means is only 20%. Thus, our results are consistent with the hypothesis that there is no dependence of the accretion rate on r_A/r_B in the limit $r_A \ll r_B$. The results also suggest that our simulations are converged. In contrast, consider the hypothesis of Perna et al. (2003) that the accretion rate scales as $(r_A/r_B)^p$ for p in the range 0.5–1. By increasing the resolution

by a factor of 4, we should have decreased r_A/r_B by a factor of 4, and thus the Perna et al. (2003) proposal predicts we should have measured an accretion rate in the range $0.044\dot{M}_B$–$0.022\dot{M}_B$ for the higher resolution simulation. This is clearly inconsistent with our results. We emphasize, however, that we have only tested the hydrodynamic case. Perna et al. (2003) made their hypothesis for both hydrodynamic and magnetohydrodynamic flows, and we have not tested the latter case.

5. CONCLUSIONS

We provide a general theoretical framework for considering problems of accretion in a medium with vorticity. Using simple analytic estimates, we have been able to derive a formula for the rate of mass accretion onto a point particle of radius r_A as a function of the vorticity present in the ambient medium. We define the dimensionless vorticity parameter ω_* as

$$\omega_* = |\omega|\frac{r_B}{c_s},\qquad(36)$$

where r_B is the accretor's Bondi radius and c_s is the sound speed. We find that the accretion rate is

$$\dot{M}(\omega_*) \simeq 4\pi\rho_\infty\frac{(GM)^2}{c_s^3}0.4f(\omega_*)\qquad(37)$$

for $\omega_* \gtrsim \omega_{\mathrm{crit}}$, where $f(\omega_*)$ is the function defined by equation (27). We note that $f(\omega_*)$ has the limiting behavior $f(\omega_*) \approx 1$ for $\omega_* \ll 1$ and that

$$f(\omega_*) \approx \frac{2}{3\pi\omega_*}\ln(16\omega_*)\qquad(38)$$

for $\omega_* \gg 1$. Simulations show that our formulation provides a good fit to the overall shape of the curve of accretion rate versus vorticity. By calibrating our first-principle calculation using the results of our simulations, we provide a formula that agrees with the mean accretion rate we measure in our simulations to better than 40%, all over 3.5 orders of magnitude variation in vorticity. Our result is a natural extension of the Bondi-Hoyle-Lyttleton formula to rotating flows.

We are also able to roughly predict several other properties of the flow, including the overall morphology, the equilibrium vorticity, and the equilibration time. Our predictions for these quantities are considerably less accurate than for the accretion rate, but our formulae are correct to within factors of a few. We see ambiguous evidence for the existence of an intermediate ω_* regime, which is characterized by a rapid change in equilibrium flow properties starting between $\omega_* = 0.1$ and $\omega_* = 10^{0.5}$. Our analytic model does not predict the existence of such a transition, and it is possible that what we have seen is a result of numerical noise. Regardless, it does seem clear that the analytic model runs into trouble when $\omega_* \sim 1$. Since we derived it for the regimes $\omega_* \ll 1$ and $\omega_* \gg 1$, and simply interpolated between those, this is not surprising.

The simulations we use to check our formulation have very general and simple initial conditions. We have avoided complications arising from boundary conditions by moving the boundaries very far away from the accreting object, and our sink particle method allows us to avoid the need for an unrealistically large accretor radius. Our theoretical discussion shows that the accretion rate is controlled by a combination of vorticity buildup near the accretor and, for $\omega_* \gtrsim 1$, the rate at which gas with low enough energy to accrete approaches the accreting particle. As a result, our results should be extremely robust.

Our results allow direct application to observed systems. One may determine the vorticity in a astrophysical system by observing a velocity gradient across it, which is often feasible using radio line observations. Consider an example in the context of star formation: Goodman et al. (1993) observed dense molecular cores in nearby star-forming regions. They found velocity gradients of ~ 0.3–3 km s^{-1} pc^{-1} in regions with typical temperatures of ~ 10 K (sound speed $c_s \approx 0.2$ km s^{-1} for a mean molecular mass of $2.33m_H$). This means that a $1\,M_\odot$ protostar ($r_B \approx 0.1$ pc) inside such a dense core has a vorticity parameter $\omega_* \sim 0.15$–1.5 [specific angular momentum $l \sim (8 \times 10^{20})$–$(8 \times 10^{21})$ g cm s^{-1}] and should have its accretion rate reduced by a factor of ~ 3–7 relative to the Bondi rate. This result has potential implications for models of star formation in which protostars gain mass through a process of competitive accretion.

APPENDIX

APPROXIMATION OF $f(\omega_*)$ FOR LARGE ω_*

We wish to derive an approximate formula for

$$f(\omega_*) = \frac{1}{\pi}\int_0^{y'_{\max}(\omega_*)}\sqrt{\frac{4 - y'^2(1 + \omega_*^2 y'^2)^2}{1 + \omega_*^2 y'^2}}\,dy'\qquad(A1)$$

in the limit $\omega_* \to \infty$. We begin by breaking it into two terms,

$$f(\omega_*) = \frac{1}{\pi}\int_0^{y'_{\max}(\omega_*)}\sqrt{\frac{4}{1 + \omega_*^2 y'^2} - y'^2(1 + \omega_*^2 y'^2)}\,dy'.\qquad(A2)$$

At the upper limit of the integration, $y' = y'_{max}$, the two terms under the square root are equal and the integrand vanishes. For smaller values of y', the first term goes to 4, while the second term scales as y'^2. Thus, the second term is significant only near the upper limit of integration. Examining Figure 1, we can see that the region $y' \approx y'_{max}$ makes only a small contribution to the integral in the large-ω_* case. Thus, we may obtain an approximation for $f(\omega_*)$ when $\omega_* \gg 1$ by dropping the second term, giving

$$f(\omega_*) \approx \frac{1}{\pi} \int_0^{y'_{max}(\omega_*)} \sqrt{\frac{4}{1 + \omega_*^2 y'^2}} \, dy' \tag{A3}$$

$$= \frac{2}{\pi \omega_*} \sin h^{-1} \left[\omega_* y'_{max}(\omega_*) \right]. \tag{A4}$$

The upper limit of integration is

$$y'_{max}(\omega_*) = \frac{3^{1/3} \left(9\omega_* + \sqrt{3 + 81\omega_*^2} \right)^{2/3} - 3^{2/3}}{3\omega_* \left(9\omega_* + \sqrt{3 + 81\omega_*^2} \right)^{1/3}}, \tag{A5}$$

which for $\omega_* \gg 1$ behaves as

$$\lim_{\omega_* \to \infty} y'_{max}(\omega_*) = \left(\frac{2}{\omega_*^2} \right)^{1/3}. \tag{A6}$$

Substituting into equation (A4), we find

$$f(\omega_*) \approx \frac{2}{\pi \omega_*} \sin h^{-1} \left[(2\omega_*)^{1/3} \right]. \tag{A7}$$

Taking the limit $\omega_* \to \infty$, this becomes

$$f(\omega_*) \approx \frac{2}{3\pi \omega_*} \ln(16\omega_*). \tag{A8}$$

Numerical integration shows that this approximation is fairly accurate over a wide range of ω_*, but the convergence is logarithmic, and the approximation does not become very good until ω_* is quite large. It is within 10% for $\omega_* > 4$ and within 5% for $\omega_* > 53$, but does not become accurate to 1% until $\omega_* > 1.8 \times 10^{12}$.

REFERENCES

Abramowicz, M. A., & Zurek, W. H. 1981, ApJ, 246, 314
Bell, J., Berger, M., Saltzman, J., & Welcome, M. 1994, SIAM J. Sci. Stat. Comput., 15, 127
Berger, M. J., & Collela, P. 1989, J. Comput. Phys., 82, 64
Berger, M. J., & Oliger, J. 1984, J. Comput. Phys., 53, 484
Bondi, H. 1952, MNRAS, 112, 195
Bonnell, I. A., Bate, M. R., Clarke, C. J., & Pringle, J. E. 1997, MNRAS, 285, 201
———. 2001a, MNRAS, 323, 785
Bonnell, I. A., Bate, M. R., & Zinnecker, H. 1998, MNRAS, 298, 93
Bonnell, I. A., Clarke, C. J., Bate, M. R., & Pringle, J. E. 2001b, MNRAS, 324, 573
DiMatteo, T., Carilli, C. L., & Fabian, A. C. 2001, ApJ, 547, 731
Fryxell, B. A., & Taam, R. E. 1988, ApJ, 335, 862
Ghez, A. M. 2004, in Coevolution of Black Holes and Galaxies, ed. L. C. Ho (Cambridge: Cambridge Univ. Press), 53
Goodman, A. A., Benson, P. J., Fuller, G. A., & Myers, P. C. 1993, ApJ, 406, 528
Hoyle, F., & Lyttleton, R. A. 1939, Proc. Cambridge Philos. Soc., 35, 405
———. 1940a, Proc. Cambridge Philos. Soc., 36, 323
———. 1940b, Proc. Cambridge Philos. Soc., 36, 325
———. 1940c, Proc. Cambridge Philos. Soc., 36, 424
Igumenshchev, I. V., & Abramowicz, M. A. 2000, ApJS, 130, 463

Igumenshchev, I. V., Abramowicz, M. A., & Narayan, R. 2000, ApJ, 537, L27
Klein, R. I. 1999, J. Comput. Appl. Math., 109, 123
Klessen, R. S., & Burkert, A. 2000, ApJS, 128, 287
———. 2001, ApJ, 549, 386
Krumholz, M. R., McKee, C. F., & Klein, R. I. 2004, ApJ, 611, 399
Melia, F. 1994, ApJ, 426, 577
Paczyński, B., & Wiita, P. J. 1980, A&A, 88, 23
Perna, R., Narayan, R., Rybicki, G., Stella, L., & Treves, A. 2003, ApJ, 594, 936
Proga, D., & Begelman, M. C. 2003, ApJ, 582, 69
Ruffert, M. 1994, ApJ, 427, 342
———. 1999, A&A, 346, 861
Ruffert, M., & Arnett, D. 1994, ApJ, 427, 351
Ruffert, M., et al. 1997, A&A, 319, 122
Sparke, L. S. 1982, ApJ, 254, 456
Sparke, L. S., & Shu, F. H. 1980, ApJ, 241, L65
Toro, E. 1997, Riemann Solvers and Numerical Methods for Fluid Dynamics: A Practical Introduction (Berlin: Springer)
Truelove, J. K., Klein, R. I., McKee, C. F., Holliman, J. H., II, Howell, L. H., Greenough, J. A., & Woods, D. T. 1998, ApJ, 495, 821
Vázquez-Semadeni, E., Ostriker, E. C., Passot, T., Gammie, C. F., & Stone, J. M. 2000, in Protostars and Planets IV, ed. V. Mannings, A. P. Boss, & S. S. Russell (Tucson: Univ. Arizona Press), 3